INVITED PAPER *Special Section on Recent Progress in Antennas and Propagation in Conjunction with Main Topics of ISAP2016*

Multi-Dimensional Radio Channel Measurement, Analysis and Modeling for High Frequency Bands

Minseok KIM[†a)], ***Member***, **Jun-ichi TAKADA**[††], ***Fellow***, ***and*** **Kentaro SAITO**[††], ***Member***

SUMMARY In order to utilize higher frequency bands above 6 GHz, which is an important technical challenge in fifth generation mobile systems, radio propagation channel properties in a large variety of deployment scenarios should be thoroughly investigated. The authors' group has been involved in a fundamental research project aimed at investigating multiple-input-multiple-output (MIMO) transmission performance and propagation channel properties at microwave frequency above 10 GHz from 2009 to 2013, and since then they have been conducting measurement and modeling for high frequency bands. This paper aims at providing comprehensive tutorial of a whole procedure of channel modeling; multi-dimensional channel sounding, propagation channel measurement, analysis, and modeling, by introducing the developed MIMO channel sounders at high frequency bands of 11 and 60 GHz and presenting some measurement results in a microcell environment at 11 GHz. Furthermore, this paper identifies challenges in radio propagation measurements, and discusses current/future channel modeling issues as future works.

key words: *radio channel, propagation, channel sounder, channel model, high frequency, millimeter-wave, MIMO*

1. Introduction

In the initial stage of developing a new wireless communication system, new aspects of propagation channel property in any new usage scenarios at a target frequency band should be elucidated for proper system design and assessment. Over recent years new spectrum use at higher frequency bands for achieving ultra-high data rates has been recognized as a key challenge in the future fifth generation (5G) mobile communications (called IMT-2020 in ITU-R). Since the multiple candidate frequency bands ranging from 24.25 GHz up to 86 GHz have been identified in the world radio conference (WRC15) [1] in 2015, the research and development are much accelerated simultaneously with standardization activities.

In 5G cellular networks, it is featured that in addition to conventional macro cells, a new radio access technology (new RAT) using a large number of small cells at higher frequency bands will be opportunistically operated to increase transmission rates and capacity to a much greater degree resolving the lack of sufficient bandwidth in conventional frequency bands [2]–[4]. The emergence of such a new deployment concept requires extending or modifying existing channel models suitable for such a new system in new environments where the channel characteristics can be much site-specific to the individual environments. Therefore, it is much obvious that realistic and accurate channel models should be very important to ensure the proper system development and evaluation, as remarked above.

Currently existing standard channel models such as 3GPP (3rd generation partnership project)/3GPP2 spatial channel model (SCM) [5], and COST2100/IC1004 [6], [7] and WINNER/3GPP [8], [9] channel models, so called, geometry based stochastic channel models (GSCM), represent the propagation channels as a sum of clustered ray paths where each path has similar propagation properties. In particular, the WINNER model is widely accepted because of their scalability and reasonable complexity, however, the frequency range is specified only from 2 to 6 GHz. Recently, in order to develop channel models for new frequency bands, various worldwide research cooperation and projects besides global standardization bodies have conducted various measurement campaigns and simulations [10]. Compiling some parts of them, in July 2016, the 3GPP released TR 38.900-Release 14 for channel models extended above 6 GHz [11] in urban macrocell (UMa), urban microcell (UMi), and indoor hotspot (InH) scenarios. However, it is recognized that a careful validation of the developed models and evaluation of modeling methodology itself should still be required due to the limited number of measurement campaigns in the rapid standardization process.

The authors' group has also been involved in a fundamental research project aimed at investigating multiple-input-multiple-output (MIMO) transmission performance and propagation channel properties at microwave frequency above 10 GHz from 2009 to 2013. Actually, 400 MHz wide bandwidth at 11 GHz was used for field experiment which is currently used for fixed wireless access (FWA) services (10.7 ∼ 11.7 GHz) in Japan [12]. We developed a fully parallel 24 × 24 MIMO channel sounder for field trials. By transmitting 64 QAM over 24 × 24 MIMO channels with 400 MHz bandwidth, it is possible to transmit above 30 Gb/s with coding rate and efficiency of 3/4 and 0.7, respectively. In Dec. 2012, the world's first 10-Gbps transmission experiments using 8 × 16 MIMO were successfully demonstrated [13], [14]. At the same time, propagation channel measurement campaigns in various indoor/outdoor environments have been extensively performed and the large scale characteristics have partly been reported in [15], [16]. When this pi-

Manuscript received February 15, 2017.
Manuscript revised June 14, 2017.
Manuscript publicized August 22, 2017.

[†]The author is with Graduate School of Science and Technology, Niigata University, Niigata-shi, 950-2181 Japan.
[††]The authors are with School of Environment and Society, Tokyo Institute of Technology, Tokyo, 152-8552 Japan.
a) E-mail: mskim@ieee.org

DOI: 10.1587/transcom.2017ISI0003

oneering work was launched, the authors were even doubtful about the success of the use of such a high frequency above 10 GHz for the mobile communication systems, recognizing the theoretical limitations of the propagation characteristics [17]. However, as mentioned above, these characteristics are taken into account rather positively in the 5G new RAT systems.

Because several excellent overview papers on radio propagation issues at millimeter-wave (mm-wave) bands, channel modeling and standardization trend for the 5G mobile communication systems are already available, e.g., in [18], [19], [21], this paper aims at providing comprehensive tutorial of the whole procedure of channel modeling; multi-dimensional channel sounder, channel measurement, analysis and modeling. In addition, the stochastic model parameters at 11 GHz compatible to the WINNER/3GPP model will be presented.

In Sect. 2, fundamentals of MIMO channel sounding is comprehensively presented from principle to implementation. Section 3 introduces our developed channel sounders in fully parallel scalable architecture, and two different configurations for 11 GHz and 60 GHz are described in detail. Then, in Sect. 4, the measurement campaigns in outdoor microcell environments at 11 GHz is introduced and the path loss characteristics obtained by polarimetric beamforming are presented. Section 5 presents a cluster based channel analysis with brief descriptions on commonly used methods of the multipath component (MPC) extraction and automatic clustering. In Sect. 6, the channel parameters are derived and the developed model will be validated with channel capacity and eigenvalue distributions with actual antenna arrays. Section 7 discusses open issues on current and future channel modeling, and identifies a few technical challenges in radio propagation measurements. Finally, Sect. 8 concludes the paper.

2. Fundamentals of Radio Channel Sounding

2.1 Sounding Principle

In order to characterize a radio propagation channel in Doppler frequency (ρ), delay (τ), and angle (Ω) domains, we acquire the samples of the channel in time (t), frequency (f), and space (d) domains, which is usually called as *channel sounding*. It is noted that the sampling domain is reversible from Fourier transform duality relationship between Doppler frequency and time, delay and frequency, and angle and space, respectively. Figure 1 illustrates the priciple of channel sounding where the sounding signal $s(t)$ with a given length and bandwidth is repeatedly transmitted and received by the antennas to acquire the propagation channel in delay, time and angle domains. The measured time varying channel impulse response (CIR) is expressed as

$$h_{\mathrm{mea}}(t,\tau,\Omega,\Omega') = g_{\mathrm{Rx}}(\tau) * a_{\mathrm{Rx}}(\Omega') * h(t,\tau,\Omega,\Omega') * a_{\mathrm{Tx}}(\Omega) * g_{\mathrm{Tx}}(\tau), \quad (1)$$

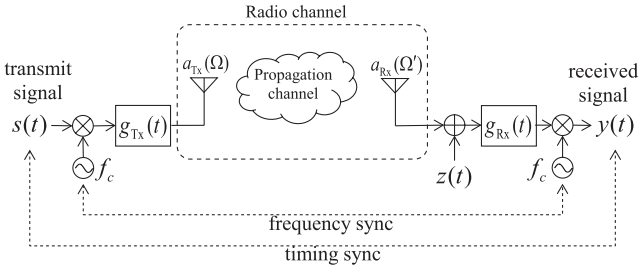

Fig. 1 Channel sounder.

where $g_{\mathrm{Tx}}(\tau)$ and $g_{\mathrm{Rx}}(\tau)$ denote transmitter and receiver responses, and $a_{\mathrm{Tx}}(\Omega)$ and $a_{\mathrm{Rx}}(\Omega')$ denote transmitter and receiver antenna responses, $h(t,\tau,\Omega,\Omega')$ denotes the true CIR, respectively. Since $g_{\mathrm{Tx}}(\tau)$ and $g_{\mathrm{Rx}}(\tau)$ are not an ideal delta function, it should be removed from the measured CIR by a deconvolution procedure (so called, back-to-back calibration). In addition, some possible hardware impairment such as the additive white Gaussian noise $z(t)$ and frequency/timing offset lead to additional error in the channel estimation [20].

Propagation channels provide an estimation of the performance of any actual hardware even if they are measured by a channel sounder which may be dedicated to very precise channel measurement but completely different from an actual hardware. Obviously, it is not necessary for propagation channels to be measured by the actual hardware as long as the hardware independent CIR can be obtained by channel sounding. Regarding the antenna deconvolution in (1), from the fact that propagation channel is uncontrollable, but antennas are designable, a *propagation channel* (or *double-direction channel*) often indicates a true channel that is separated from the influence of antennas, i.e., $a_{\mathrm{Tx}}(\Omega)$ and $a_{\mathrm{Rx}}(\Omega')$, and we often distinguish that from a *radio channel* (or *MIMO channel*, if necessary) [21], [22].

A radio channel can of course be achieved by using general-purposed instruments such as a vector network analyzer (VNA) and a spectrum analyzer (SA). However, multi-dimensional channel sounders based on wideband signaling through a MIMO antenna array, e.g., commercial products such as Medav RUSK MIMO channel sounder [23], Elektrobit Propsound [24] and KODEN channel sounder [25], and lots of custom developments [26]–[31] are usually used for fast and accurate channel acquisition.

2.2 Sounding Signal Design for Delay Domain Channel Acquisition

As described above, a wideband signal is usually used for fast acquisition of delay domain characteristics. A sequence of short pulses as close as to an impulse signal with very short duration that determines the delay resolution can be considered. However, in the signal design for wideband radio channel measurements, low peak-to-average power ratio (PAPR) or crest factor (CF) at the transmitter is a great concern to release the back-off margin of power amplifiers. To

achieve low crest factor, it is desirable for the signal waveform to have a constant envelope. At the same time, it is preferable that they have uniform excitation property in frequency domain for the same quality of the channel estimation and the power efficiency.

As a realization of signal waveform with low crest factor, Newman phase multitone (NPM) [23], [26], [34] and Zadoff-Chu sequence (ZCS) [32], [35] have been employed in many systems because of its excellent properties with respect to the above requirements. This subsection describes two widely used signals of an NPM as a frequency domain sequence that estimates a channel transfer function (CTF), and a ZCS as a time domain sequence that estimates a CIR.

A continuous time bandpass representation of a multitone signal waveform can be written as

$$x(t) = \sqrt{\frac{2}{N}} \sum_{m=-N/2}^{N/2-1} \cos\left[2\pi(f_c + m\Delta_F)t + \phi_{m+\frac{N}{2}}\right], \quad (2)$$

where f_c is the center frequency and $\phi_k \triangleq \frac{\pi k^2}{N}$ for $k = 0, ..., N-1$, which is a phase term developed for the crest factor reduction [34]. Δ_F and N denote the tone spacing and the number of tones (even number) to be allocated across the given frequency band ($N\Delta_F$). The crest factor of $x(t)$, $\mathrm{CF}(x)$ is defined by $\frac{\|x\|_\infty}{\|x\|_2}$ where $\|x\|_\infty$ and $\|x\|_2$ are the maximum absolute value and root-mean-square (rms) value of $x(t)$, respectively. Using Parseval's theorem, the rms value of (2) can be simply calculated by 1 from the perfect uniform spectrum of the signal [34]. However, although $\|x\|_\infty$ has not been obtained by a closed form solution, the crest factor of (2) has been shown about 4.7 dB with moderate number N by numerical results [34].

The signal waveform in (2) can be rewritten as

$$x(t) = \sqrt{2} \cdot \mathrm{Re}\left[s(t) \exp\left(\mathrm{j}2\pi f_c t\right)\right], \quad (3)$$

where

$$s(t) = \frac{1}{\sqrt{N}} \sum_{m=-N/2}^{N/2-1} \exp\left(\mathrm{j}2\pi m\Delta_F t\right) \Psi_{m+N} \quad (4)$$

which is the equivalent complex baseband representation of (2) where $\Psi_k = \exp\left(\mathrm{j}\phi_k\right)$ which is the complex NPM sequence in frequency domain. Then, the discrete time version of (4) can be represented by

$$\begin{aligned} s_n &= \frac{1}{\sqrt{N}} \sum_{m=-N/2}^{N/2-1} \exp\left(\mathrm{j}\frac{2\pi nm}{N}\right) \Psi_{m+N} \quad (5) \\ &= \frac{1}{\sqrt{N}} \sum_{k=0}^{N-1} \Psi_{k+\frac{N}{2}} \exp\left(\mathrm{j}\frac{2\pi n}{N}\left(k + \frac{N}{2}\right)\right), \end{aligned}$$

which indicates $S_k = \Psi_{k+\frac{N}{2}}$ where S_k denotes discrete Fourier transform (DFT) of s_n. Namely, the time sequence of (5) is obtained by the inverse DFT (IDFT) of the $N/2$ cyclically shifted version of the original complex NPM sequence.

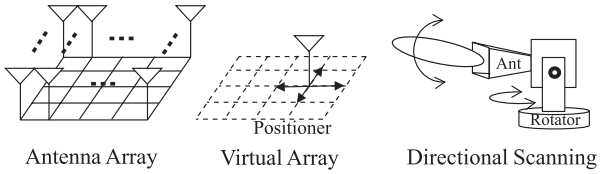

Fig. 2 Angle domain channel acquisition schemes.

On the other hand, as a constant amplitude zero auto-correlation (CAZAC) sequence, D. Chu developed so called Zadoff-Chu sequence (ZCS) [35] which is defined by

$$z_n \triangleq \begin{cases} \exp\left(-\mathrm{j}\frac{\pi\eta n^2}{N}\right) & N \text{ even} \\ \exp\left(-\mathrm{j}\frac{\pi\eta n(n+1)}{N}\right) & N \text{ odd}, \end{cases} \quad (6)$$

where N denotes the length of the sequence, and η is relatively prime to N. (6) is periodic function with period N. It is currently used for synchronization in 3GPP LTE systems owing to its excellent auto-correlation property [32]. It should be noted that the IDFT of the complex NPM is identical to the ZCS with $\eta = 1$ multiplied by a constant number [37].

2.3 Measurement Schemes for Angle Domain Channel Acquisition

For angle domain channel acquisition, we usually have three options; a full array, a virtual array and directional antenna scanning as shown in Fig. 2. In the full array configuration, simultaneous transmission from multiple antennas using orthogonal waveforms should be available, which leads to fast acquisition in space domain but is generally complex and costly to implement. On the other hand, the virtual array configuration can capture the channel in space domain with a single antenna element which has to be physically moved to multiple positions to form a full array (a synthetic array), which usually requires a long measurement time but can be configured in relatively low cost. In these two methods mentioned above, the channel responses in angle domain are usually obtained by array signal processing such as beamforming which is equivalent to Fourier transform of the space domain samples.

Lastly, especially for high frequency channel measurement, e.g., at mm-wave bands, the use of directional antenna scanning in which any array signal processing is unnecessary is a popular method because the full array is very costly and the virtual array often suffers from the phase drift for a very long measurement time due to the relatively high phase noise of local oscillators at mm-wave frequency [31], [44]. In the virtual array as well as the directional antenna scanning, the channel is assumed to be static during the measurement. A long measurement time usually limits the measurement capability for Doppler characteristics in dynamic scenarios.

2.4 MIMO Multiplexing Schemes

As described above, a full array scheme offers a fast channel

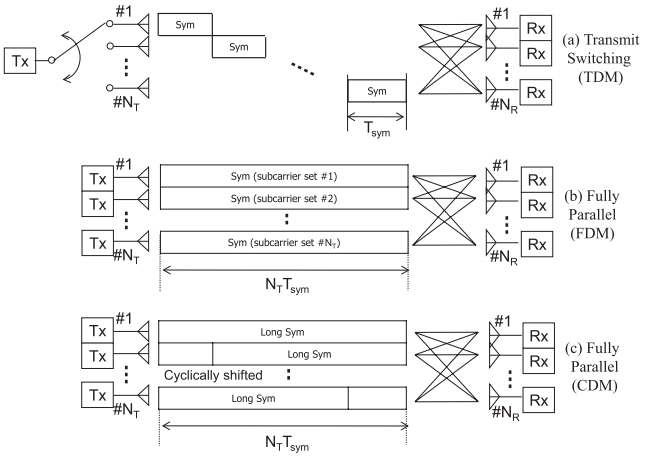

Fig. 3 MIMO channel sounding schemes.

acquisition in space domain by simultaneous multiple signal transmission and reception, which needs a proper multiplexing scheme for separating all transmitted signals from multiple antennas at the receiver. The transceiver architecture of a MIMO channel sounder determines the multiplexing scheme as will be described in the following. Figure 3 shows three possible MIMO channel sounder schemes where basically TDM (time division multiplexing) [23], [26]–[28], FDM (frequency division multiplexing) [38], [39], and CDM (code division multiplexing) [40], [41] schemes or a hybrid method among them can be chosen appropriately.

2.4.1 Transmit Antenna Switching Architecture

First, in order to reduce the implementation cost, a transmitter switching architecture that has a single radio front-end at the transmitter, and a single (fully switching) radio front-end [23], [28] or a complete set of antennas and radio front-ends (semi-parallel scheme) [42] at the receiver as shown in Fig. 3(a) is widely employed with a TDM scheme. The TDM scheme sequentially transmits the signal at each antenna adding a appropriate guard interval in between, thus it usually takes a long measurement time but provides an easy maintenance and calibration from the simple architecture of the corresponding hardware.

2.4.2 Fully Parallel Architecture

Consider a fully parallel architecture that has complete sets of antennas and radio front-ends at both the transmitter and receiver [38], [43] employing FDM and CDM schemes with NPM sequence respectively.

The NPM sequence can be multiplexed by frequency shifted orthogonal data set at every antenna [38] for MIMO channel sounding, so called a FDM scheme. By using (5), the FDM sequence for l-th transmit antenna ($l = 1, \ldots, N_{\mathrm{T}}$) is expressed by

$$s^{(l)}_{\mathrm{FDM}}[n'] = s_{\mathrm{mod}(n',N)} \exp\left(\mathrm{j}\frac{2\pi(l-1)n'}{N_{\mathrm{T}}N}\right) \tag{7}$$

for $n' = 0, \ldots, N_{\mathrm{T}}N - 1$ where $\mathrm{mod}(a, b)$ is the remainder of a divided by b.

On the other hand, in the previous sections, we found that the zero auto-correlation property of the complex NPM sequence can also be applied to the CDM scheme, since it is a special case of the ZC sequence. The l-th antenna transmits the cyclically shifted version of the original sequence by $(l-1)N$, respectively, which means the signal length should be N_{T} times of the original signal length, namely $N_{\mathrm{T}}N$. At receiver side, each can be separated by cross-correlation with the original sequence. Figure 3(b) and (c) illustrate the FDM and CDM schemes, respectively.

The fully parallel architecture can reduce the measurement time per snapshot by only $1/N_{\mathrm{R}}$, where N_{R} denotes the number of receive antennas. As shown in Fig. 3, it should be noted that the fully parallel architecture cannot reduce the measurement time any further because simultaneous transmission requires a repetitive transmission of an original signal or long symbol duration for the number of signals to be transmitted simultaneously for signal separation on the receiver side.

3. MIMO Channel Sounder Hardware

This section describes the fully parallel scalable MIMO channel sounders at 11 GHz and 60 GHz developed by Tokyo Tech. [29], [38] and jointly developed by Niigata University and Tokyo Tech. [44], respectively.

3.1 Fully Parallel Scalable Architecture

The demands on multiple link communications among more than two nodes that are spatially distributed over large areas are increasing to significantly improve MIMO transmission performance. Emerging applications using this multi-link (ML) technique include multi-user (MU) MIMO, base station cooperation which is also known as cooperative multipoint (CoMP) [48], distributed antenna systems (DAS), etc. In particular, the design and analysis require more sophisticated channel models for fading correlation among the multiple links based on the high-resolution subspace structure of each link [18], [49]. In multiple antenna systems, it is essential to investigate channel subspace structure which can only be known from the spatial (directional) channel properties. Then, we can predict the possible channel ranks and design the optimum MIMO array antenna as well as the appropriate system parameters.

To measure ML channels accurately a dedicated architecture suitable for flexible configuration for various ML situations and sufficiently robust against a few problems of implementing distributed systems such as synchronization is necessary. A scalable channel sounding architecture and an efficient signal processing technique [38] may offer a most practical and reliable solution. The developed scalable architecture based on a modular transceiver concept is illustrated in Fig. 4. That enables an easy extension with new units, easy combination with multiple units for single-link (SL) di-

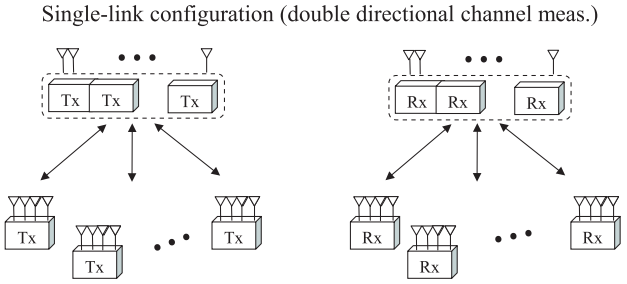

Fig. 4 Scalable MIMO channel sounding concept.

rectional channel measurement, and easy spatial separation into multiple units for ML MIMO channel measurement. Each unit can work independently and can be incorporated in a complete system as a sub-system. In addition, the fully parallel transceiver architecture allows the same hardware to be shared or simultaneously used for the transmission test as well, which is an important advantage.

3.2 Frame Format and System Specifications

For the fully parallel scalable architecture consisting of multiple units, a scalable frame format is presented in Fig. 5. It consists of a preamble, transmission symbols (T-symbols) and propagation symbols (P-symbols). Each number of symbols is equal to the number of the transmitter units (N_{Utx}) where each unit has four antennas. The preamble and T-symbols are flexibly used for the MIMO-OFDM transmission test, and the P-symbols are designed to be four times longer than the preamble or T-symbol for detail channel analysis with long measurable delay span, where the same hardware platform can be shared for both purposes of transmission test and directional channel measurement.

For channel sounding by P-symbols, the FDM and STDM (space-time division multiplexing) layered scheme has been developed as shown in Fig. 6. Regarding the FDM, the complex envelope of each transmit signal within the same transmitter unit can be expressed by (7). Then, to further multiplex the same FDM channel signals from different transmitter units, transmit orthogonal beamforming is performed N_{Utx} times with $\boldsymbol{w}^{(m)} \in \mathbb{C}^{N_{\mathrm{Utx}} \times 1}$ which is an orthogonal weight vector for the m-th STDM slot with unit gain ($m = 1, \ldots, N_{\mathrm{Utx}}$). This allows simultaneous transmission for all transmit antennas, and hence offers a processing gain in SNR, i.e., beamforming gain. As a result, the transmission power per transmit antenna can be maintained relatively small [38].

The specifications of the developed system are given in Table 1, which has been developed for multiple purposes of propagation channel characterization and MIMO-OFDM transmission test in various SL and ML scenarios. In this development, to realize data transmission throughput above 30 Gbps, using a wideband signal of 400 MHz at 11 GHz it can be configured up to a 24×24 MIMO system (6 Tx and 6 Rx units having four antennas each).

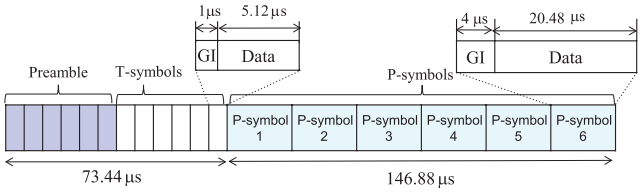

Fig. 5 Frame format for 6 transmitter units.

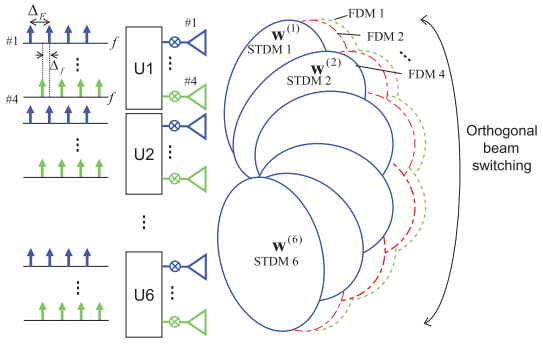

Fig. 6 FDM-STDM layered multiplexing for channel sounding (P-symbols).

Table 1 Specifications of 11 GHz sounder.

Basic signal parameters	
Carrier frequency	11 GHz
Signal bandwidth ($2B$)	400 MHz
Sampling rates (f_s)	800 MHz
No. tones/subcarriers (N)	2, 048
Carrier spacing (Δ_F)	195 kHz
FFT length (N)	4, 096
GI length (N_{GI})	800
Preamble and T-symbol	
T-symbol duration (T_{T})	6.12 μs
Payload duration	5.12 μs
GI duration	1 μs
P-symbol	
P-symbol duration	24.48 μs
Payload duration	20.48 μs
GI duration	4 μs
FDM tone spacing (Δ_f)	48.8 kHz
Scalable frame format	
Multiplexing scheme	STDM
No. Tx units (N_{Utx})	1 ~ 6 (scalable)
No. Rx units (N_{Urx})	1 ~ 6 (scalable)
No. ant. per unit (N_A)	4
No. Preamble symbols No. T-symbols No. P-symbols	N_{Utx}
Frame duration	36.72 ~ 220.32 μs

3.3 Sub-Systems and Synchronization

The developed sub-system, a part of the full system, is equipped with eight parallel transmitter/receiver chains using two units based on a generic SDR platform as shown in Fig. 7 [29]. The sub-system is composed of a couple of RF and basedband boards, and a clock-trigger and a CPU board in a CompactPCI card slot. The photographs of the rack

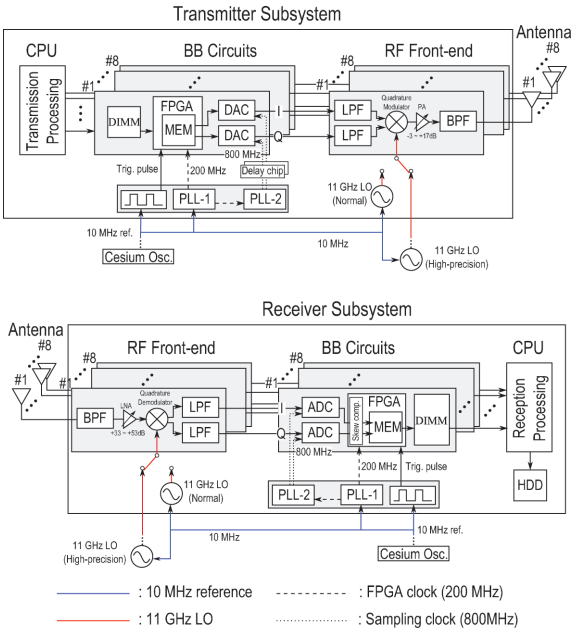

(a) Block diagram [29].

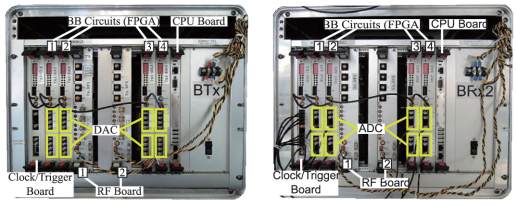

(b) Sub-system chassis.

Fig. 7 A developed sub-system with eight antennas using two units.

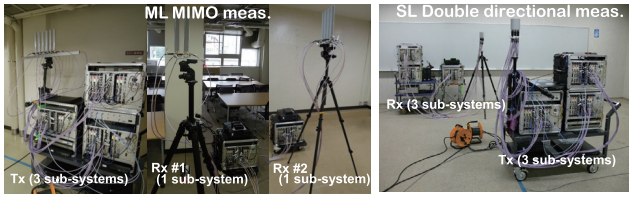

Fig. 8 ML (left) and SL (right) measurement scenes.

mount chasses are shown in Fig. 7. The baseband boards mainly consist of FPGAs, ADCs/DACs, and large DIMMs (4 GB per channel). The skew among the DACs and the ADCs over all sub-systems can be compensated by using programmable delay chips with 10-ps precision. As for the RF boards, both of the quadrature up-/down-converters were developed based on a direct conversion architecture because it can be realized in low-cost and small-volume. However, the direct conversion architecture is typically sensitive to the I/Q imbalance and carrier leakage that should be carefully compensated before beginning the measurements [54].

Figure 8 illustrates the ML and the SL measurement scenes. In the ML measurement setup with multiple Tx and Rx sub-systems, the master PC remotely controls all sub-systems via LAN/Wi-Fi. The system clock of each sub-system is generated from the 10 MHz reference signal from the external Cesium oscillator for synchronization among the sub-systems. In addition, an external high-precision local oscillator (LO) is used to reduce the harmful effect of phase noise on the channel estimation. In each sub-system, transmission and reception of the measurement block of snapshots (the specified number of consecutive measurement data frames) are executed based on the internally generated trigger pulse, and all trigger pulses of each sub-system are synchronized in the calibration procedure via cable connection before the sub-systems will be physically separated. The trigger pulse synchronization relies on the stability of the reference clock. As described above, in the developed system Cesium atomic oscillator [50] is used, but it should be noted that the trigger offset of approximately 0.77 ns/hour maximum between sub-systems are still observed [29], which means that a measurement campaign for a long time without calibration cannot be admitted. A precise synchronization should still be a technical challenge.

3.4 Calibration

As in the transmission performance in wireless systems, the measurement accuracy of channel sounders is degraded due to various hardware imperfections such as ADCs'/DACs' skew and amplitude mismatch [51], RF transceiver's I/Q mismatch, carrier leakage [52]–[54], and nonlinearity [51], LO's phase noise, frequency error [51], [55], etc. Since the channel sounder has fully parallel transceiver architecture, a precise calibration is needed for accurate multi-dimensional high-resolution channel measurement. In the developed system, the calibration procedure includes a trigger pulse synchronization, a baseband circuit adjustment such as ADC/DAC channel skew, an RF circuit compensation such as I/Q imbalance and carrier leakage, and a back-to-back measurement to remove the system transfer characteristics from the measured channel responses.

In case of 24×24 MIMO configuration, the procedure includes

- Trigger pulse synchronization among six sub-systems
- Skew adjustment for 48 ADCs and 48 DACs (not necessary to do this in every time)
- I/Q imbalance and carrier leakage compensation for 24 up-converters and 24 down-converters
- Back-to-back measurements for all MIMO connections (576 measurements)

which indeed takes huge amount of time. As described above, the requirement of a huge number of operations for calibration is a significant drawback of fully parallel transceiver architecture. For fast and efficient calibration, a series of automatic processing for each step has been developed [29]. Among them, it is noted that the back-to-back measurements consumes most of the time (straightforwardly a few hours including the time needed for switching cable

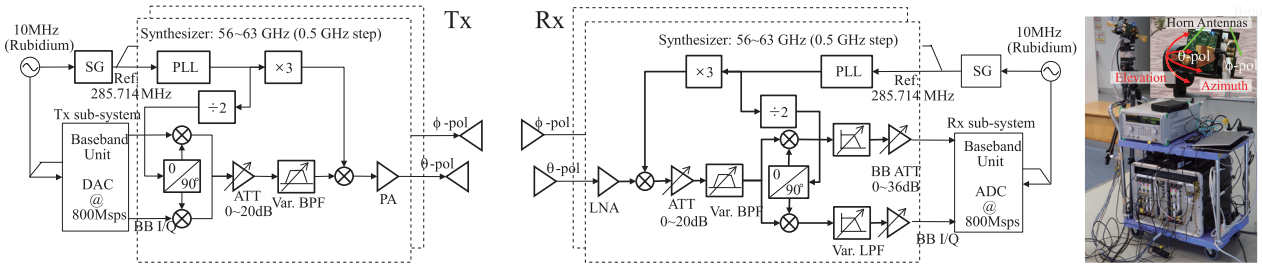

Fig. 9 Schematic diagram and photograph of 60 GHz MIMO channel sounder.

connection). During the back-to-back measurement from beginning to end, even very small frequency difference possibly existing among the atomic reference clocks of each sub-system leads to significant phase rotation over time. The error in the transfer functions due to the trigger timing offset is corrected by an offline processing.

3.5 Modification into 60 GHz mm-wave MIMO Channel Sounder

Based on the platform of the above mentioned subsystem, a 60 GHz mm-wave MIMO channel sounder has been developed [31], [44]. The RF transmitter and receiver were replaced by a commercial mm-wave product (V60TXWG1/V60RXWG1, VubIQ [56]) which integrates waveguide module with standard WR15/WG25 flange interfaces. The waveguide module incorporate SiGe BiCMOS radio chips with the ability to produce 12 dBm P1dB transmit output power and 6 dB receiver noise figure. The channel sounder is configured in 2×2 MIMO to measure full polarimetric CTFs simultaneously.

As illustrated in Fig. 9, the RF transceivers employ a heterodyne IF architecture with variable frequency IF and RF mixers for different RF channel selection, which requires a single common synthesizer for IF and RF LO signal generation. In the typical setup, the baseband signal input power is adjusted by approximately −13 dBm, so that the transmit power of approximately 10 dBm is achieved by power amplification of 23 dB. We exclude the influence of the measurement system from the measured channel responses by full MIMO back-to-back calibration (direct cable connection between Tx and Rx antenna ports with a waveguide and an attenuator). The measurement dynamic range is limited to approximately 30 dB.

Because the phase noise of the RF transmitter/receiver was relatively large [31], the FDM is disadvantageous because it needs a long symbol duration for multiplexing. It is noted that as shown in Fig. 3, the TDM scheme just transmits the sounding symbol from each antenna sequentially, but the FDM scheme needs to increase the frequency resolution of the original sounding symbol by the number of FDM channels in order to separate each channel by discrete Fourier transform at the receiver, which leads to long sequence in time domain. Therefore, we modified the FDM frame structure into TDM scheme to reduce the symbol duration per channel as shown in Fig. 10(b) where it is reduced by 1/8 of

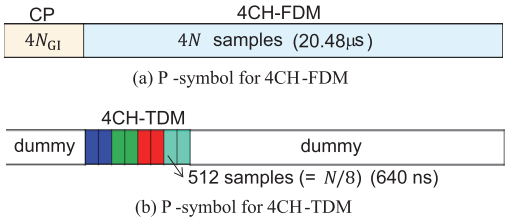

(a) P -symbol for 4CH-FDM

(b) P -symbol for 4CH-TDM

Fig. 10 P-symbol formats for FDM and TDM.

Table 2 Specifications of 60 GHz channel sounder.

Carrier frequency	58.5 GHz
Signal bandwidth	400 MHz
Sampling rates (f_s)	800 MHz (R_{ov}=2)
Sounding signal	Unmodulated multitone (No. tones (N) = 256)
FFT length	512 ($N/8$)
Tone spacing (Δ_F)	1.563 MHz
Delay resolution	2.5 ns
Maximum delay	640 ns
Multiplexing scheme	TDM
No. Tx ant.	2 (θ/ϕ orthogonal dual-polarization)
No. Rx ant.	2 (θ/ϕ orthogonal dual-polarization)

the original FDM symbol length shown in Fig. 10(a). It is noted that only two TDM symbols are actually used for 2×2 MIMO.

Full polarimetric double-directional CTFs are acquired by directional antenna scanning, where two orthogonally polarized (θ and ϕ) high gain horn antennas are used at both sides of Tx and Rx, where those antennas are not co-located but direct toward the opposite direction (180 degrees) on the same plane as shown in the photograph of Fig. 9 to save the measurement time. Because the half power beam-width (HPBW) is 12 degrees (24 dBi gain), the azimuth and elevation angles are typically varied in 12 degree steps. The indoor/outdoor measurement campaigns have been conducted, but the channel modeling is still on-going [44]–[47].

4. Measurement Campaign

In this section, the measurement campaign for outdoor channels at 11 GHz is described and the large scale characteristics obtained from the measured data are presented.

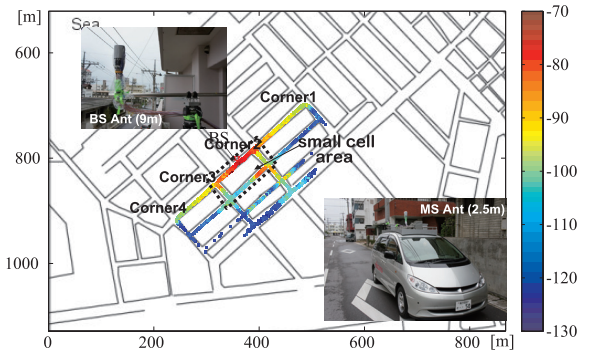

Fig. 11 Measurement course where BS antenna is installed in balcony of apartment (3rd floor).

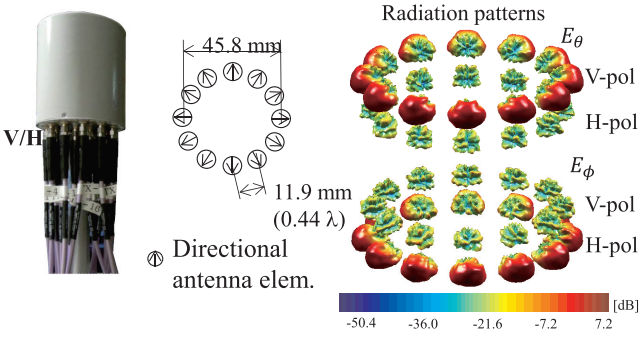

Fig. 12 UCA antenna and measured 3-D radiation patterns.

4.1 Measurement Description

The field measurements in an UMi environment that was mainly a residential area with cell radius of approximately 200 m has been conducted in Ishigaki city, Okinawa, Japan. Figure 11 indicates the map of the measurement route. The Rx antenna array as a base station (BS) was installed in the 3rd floor of an apartment approximately 9 m above the ground (slightly higher than the average building height). The Tx antenna array was installed on top of the measurement vehicle as a mobile station (MS), and the antenna height was approximately 2.5 m. The snapshots were taken at constant time interval while MS was moving at the velocity slower than 10 km/h. Regarding the antenna array, the orthogonally dual-polarized 12-element uniform circular arrays (UCA) as shown in Fig. 12 where each antenna element has the gain of 7 dBi, were used at both sides of Tx and Rx. Double-directional azimuth angle delay power spectra (ADPS) were obtained by polarimetric beamforming with the precise 3-D antenna element patterns as described below. Figure 11 also indicates the measured path gain on the measurement route.

4.2 Polarimetric Beamforming for Synthetic Omni-directional Path Gain

Angle-resolved polarimetric CTFs are obtained by polarimetric beamforming to the measured MIMO CTFs with the array responses as

$$\boldsymbol{G}(f,\phi,\phi') = \begin{bmatrix} G_{\mathrm{VV}}(f,\phi,\phi') & G_{\mathrm{VH}}(f,\phi,\phi') \\ G_{\mathrm{HV}}(f,\phi,\phi') & G_{\mathrm{HH}}(f,\phi,\phi') \end{bmatrix} \quad (8)$$

$$= \boldsymbol{W}'^{H}(f,\phi')\boldsymbol{H}(f)\boldsymbol{W}^{*}(f,\phi), \quad (9)$$

where the beamforming weights, $\boldsymbol{W}^{*}(f,\phi) = \left(\boldsymbol{A}^{T}(f,\phi)\right)^{+}$, and $\boldsymbol{W}'^{H}(f,\phi') = \left(\boldsymbol{A}'(f,\phi')\right)^{+}$ with the superscript $^{+}$ denoting Moore-Penrose pseudo-inverse of a matrix. The matrices of the polarimetric antenna pattern $\boldsymbol{A}(\phi) \in \mathbb{C}^{24\times 2}$ and $\boldsymbol{A}'(\phi') \in \mathbb{C}^{24\times 2}$ for the Tx and Rx are constructed, respectively, as

$$\boldsymbol{A}(f,\phi) = \left[\begin{array}{c|c} \boldsymbol{a}_{\mathcal{V},\mathrm{V}}(f,\phi) & \boldsymbol{a}_{\mathcal{V},\mathrm{H}}(f,\phi) \\ \boldsymbol{a}_{\mathcal{H},\mathrm{V}}(f,\phi) & \boldsymbol{a}_{\mathcal{H},\mathrm{H}}(f,\phi) \end{array}\right], \quad (10)$$

$$\boldsymbol{A}'(f,\phi') = \left[\begin{array}{c|c} \boldsymbol{a}'_{\mathcal{V},\mathrm{V}}(f,\phi') & \boldsymbol{a}'_{\mathcal{V},\mathrm{H}}(f,\phi') \\ \boldsymbol{a}'_{\mathcal{H},\mathrm{V}}(f,\phi') & \boldsymbol{a}'_{\mathcal{H},\mathrm{H}}(f,\phi') \end{array}\right], \quad (11)$$

where ϕ indicating the azimuth AoD (angle of departure) at the Tx and ϕ' indicating the azimuth AoA (angle of arrival) at the Rx. The component column vectors in the right term of (10) indicate

$\boldsymbol{a}_{\mathcal{V},\mathrm{V}}$: V polarization's directivity of VP element,
$\boldsymbol{a}_{\mathcal{V},\mathrm{H}}$: H polarization's directivity of VP element,
$\boldsymbol{a}_{\mathcal{H},\mathrm{V}}$: V polarization's directivity of HP element,
$\boldsymbol{a}_{\mathcal{H},\mathrm{H}}$: H polarization's directivity of HP element,

and those in the right term of (11) is explained in the same manner. For (9), the co-elevation angles (zenith) at Tx and Rx were determined by the antennas' heights and the distance between Tx and Rx, then, the azimuth beamforming on that resulting elevation plane was actually performed.

The polarimetric CIRs of g_{qp} are obtained by IDFT of G_{qp} in (8). Replacing the values below the noise level with zero, the synthetic omni-directional average path gain for 'qp' polarization is calculated as

$$\hat{P}_{\mathrm{qp}} = \frac{1}{\zeta'}\frac{1}{\zeta}\sum_{\tau=0}^{N-1}\sum_{n=0}^{Q'-1}\sum_{m=0}^{Q-1}\left|g_{\mathrm{qp}}(\tau,\phi_m,\phi'_n)\right|^2. \quad (12)$$

where $\zeta = W/\Delta_\phi$ and $\zeta' = W'/\Delta'_\phi$ denote the gain correction constants where W and W' denote the 3-dB beam width of the beamformer which are approximately 24° in the used UCA, and Δ_ϕ and Δ'_ϕ denote the resolution of the angular power spectra for AoD and AoA, respectively (herein, $\Delta_\phi = \Delta'_\phi = 6°$), and Q and Q' denote the number of angular samples (herein, $Q = Q' = 60$). It should be noted that the antenna beam pattern effect is not perfectly removed by (12) and the results for vertical polarization at both Tx and Rx will be presented hereafter.

4.3 Path Loss

As described above, using the angle-resolved CTFs by polarimetric beamforming, the omni-directional path gain is

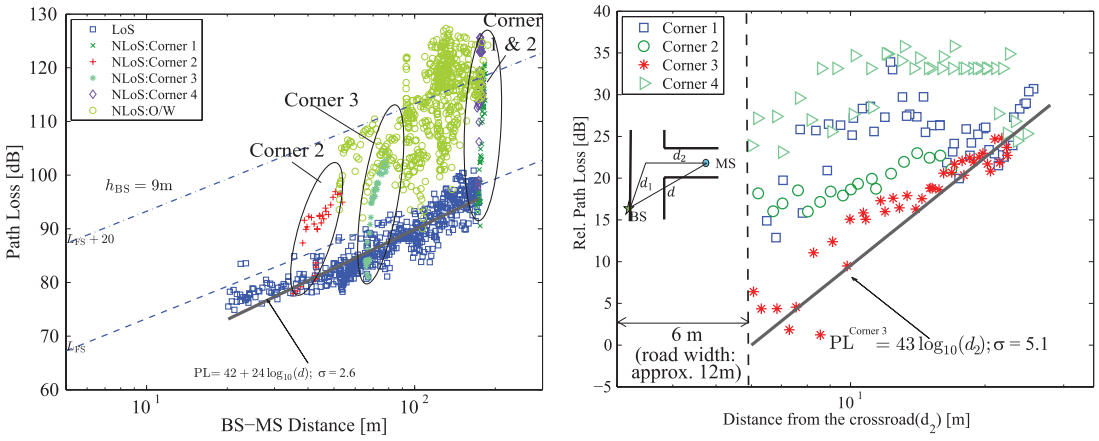

(a) PLs for LoS and NLoS. (b) PL beyond corner.

Fig. 13 Measured path gain versus distance (VV).

Table 3 Path loss models for UMi.

	Scenarios	Model	Shadowing	Condition
11 GHz	LoS	$PL_{LoS}(d) = 42.0 + 24.0 \log_{10} d$	$\sigma = 2.6$	$20 < d < 180$ [m] $h_{BS} = 9$, $h_{MS} = 3$
	NLoS	$PL = PL_{LoS}(d_1) + 43 \log_{10} d_2$	$\sigma = 5.1$	Corner #3 $d_2 > w/2$ [m] for $w = 12$ $h_{BS} = 9$, $h_{MS} = 3$
3GPP UMi [9] (f_c = 11GHz)	LoS	$PL_{LoS}(d) = 48.8 + 22.0 \log_{10} d$	$\sigma = 3.0$	$10 < d < d_{bp}$ [m] $h_{BS} = 10$, $h_{MS} = 1.5$
	NLoS	$PL = PL_{LoS}(d_1) - 12.9 + 27.3 \log_{10} d_2$	$\sigma = 4.0$	perpendicular street ($w = 20$) $10 < d_1 + d_2 < 5000$ [m] $h_{BS} = 10$, $h_{MS} = 1.5$

synthesized. Figure 13(a) shows the path loss (PL) characteristics for vertical polarization along the ground distance between Tx and Rx. It is observed that the path loss exponent (PLE) in line-of-site (LoS) condition is $a = 2.4$ with $d > 20$ m, and in non-line-of-site (NLoS) conditions the PLs are widely distributed between L_{FS} and $L_{FS} + 20$ dB for $d < 100$ m where L_{FS} denote the free space path loss.

In addition, the ovals in Fig. 13(a) denoted by Corner 1 ~ Corner 4 indicate the measured PLs beyond the corners of which locations are illustrated in Fig. 11. For characterizing the corner attenuation, an additional loss for the distance from the center of the crossroad was introduced [8], [9]. Depending on the types of the corner objects and the LoS distance from the BS, the attenuation trend is largely different as shown in Fig. 13(b) where the value in y-axis denotes the normalized path loss in terms of that at the crossroad and $d_2 > w/2$ (a half of the road width w). d_1 and d_2 are the distances from the BS to the center of the crossroad, and from the center of the crossroad to the MS along the perpendicular street. The PLE of the path loss in the corner 3 ($d_1 \approx 37.4$ m) was 4.3 where the dominant mechanism is thought to be the propagation along the street. The path loss models are summarized in Table 3 where $f_c = 11$ GHz was applied to the 3GPP UMi model [9] for comparison.

5. Channel Analysis

This section briefly describes cluster based channel analysis and presents the derived channel model parameters compatible to the WINNER/3GPP GSCM model [8], [9] for small cell micro cellular environments.

5.1 Small Cell Measurement Course

Figure 14(a) indicates the measurement course on the 3-D model. This course is a part of the measurement course for 10 Gbps outdoor transmission field experiments [13] where it was in LoS and NLoS mixed conditions. The markers of 'o' and '×' on the course map indicate LoS and NLoS conditions, respectively. The MS points between #0 and #39 are in NLoS condition due to the blockage by the houses on the left side of the MS vehicle moving in right direction. The points between #40 and #63 nearby the open space and the parking lot are in LoS condition. At the points between #64 and #85 it is changed into NLoS due to the blockage by the building around the corner. Then, at the points from #86 to #143 it is changed again into LoS. The physical structure of the environment can be checked by the panoramic view from the BS as shown in Fig. 14(b). The typical power delay profiles (PDPs) in each condition are illustrated in Fig. 15.

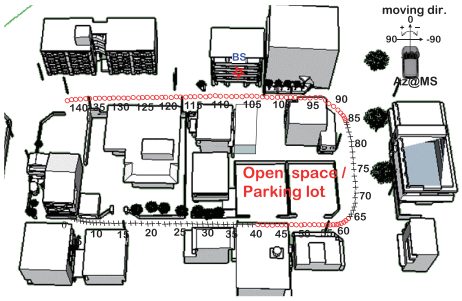

(a) Course 3-D map.

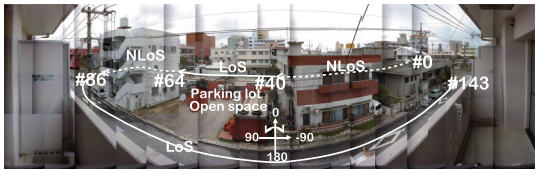

(b) Panoramic view from BS (3rd floor of the apartment).

Fig. 14 Small cell measurement course.

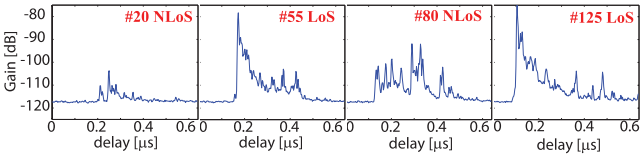

Fig. 15 Typical PDP for each area.

5.2 MPC Extraction and Automatic Clustering

The measured MIMO channel matrix at the specific frequency is ideally described as

$$\boldsymbol{H}_{\text{mea}} = \boldsymbol{H}_{\text{model}}(\boldsymbol{\mu}, \boldsymbol{\Gamma}) + \boldsymbol{Z} \tag{13}$$

where $\boldsymbol{Z}$ denotes addictive white Gaussian process, the MPC parameter set, $\boldsymbol{\mu} = [\boldsymbol{\mu}_1^T, ..., \boldsymbol{\mu}_L^T]^T$, and the complex path weight, $\boldsymbol{\Gamma} = [\boldsymbol{\Gamma}_1^T, ..., \boldsymbol{\Gamma}_L^T]^T$. The model is assumed to be a superposition of L separable number of plane wave MPCs as

$$\boldsymbol{H}_{\text{model}}(\boldsymbol{\mu}, \boldsymbol{\Gamma}) = \sum_{l=1}^{L} \boldsymbol{A}'(\boldsymbol{\Omega}_l')\boldsymbol{\Gamma}_l \boldsymbol{A}^T(\boldsymbol{\Omega}_l) e^{-\mathrm{j}2\pi f \tau_l}, \tag{14}$$

where $\boldsymbol{A}(\boldsymbol{\Omega}_l)$ and $\boldsymbol{A}'(\boldsymbol{\Omega}_l')$ denote the dual-polarized antenna pattern matrix ($\in \mathbb{C}^{24\times 2}$) for the Tx and Rx, respectively as described in Sect. 4. Here, the MPC parameters $\boldsymbol{\mu}_l = [\tau_l, \boldsymbol{\Omega}_l, \boldsymbol{\Omega}_l']^T$ where $\boldsymbol{\Omega}_l = [\theta_l, \phi_l]$ indicating the azimuth and co-elevation AoD at the Tx and $\boldsymbol{\Omega}_l' = [\theta_l', \phi_l']$ indicating the AoA at the Rx. The complex path weight is defined by $\boldsymbol{\Gamma}_l = \begin{bmatrix} \gamma_{l,\text{VV}} & \gamma_{l,\text{VH}} \\ \gamma_{l,\text{HV}} & \gamma_{l,\text{HH}} \end{bmatrix}$.

From (13) the optimum MPC parameters can be obtained by the following maximum likelihood estimation (MLE) by minimizing the negative log-likelihood function as

$$\boldsymbol{\mu}_{\text{opt}} = \arg\min_{\boldsymbol{\mu}} ||\boldsymbol{H}_{\text{mea}} - \boldsymbol{H}_{\text{model}}(\boldsymbol{\mu})||_F^2, \tag{15}$$

where $\|\cdot\|_F$ denotes Frobenius norm. However, (15) leads to an enormous computational complexity to find the optimum multi-dimensional parameters of L MPCs if L increasing. Therefore, to relax the computational complexity some modified MLEs have been implemented using iterative methods such as SAGE (space alternative generalized expectation maximization) algorithm [58], RIMAX (Richter maximum likelihood estimation) [59], etc.

The recent standard approaches of channel modeling [5]–[9] are based on cluster rather than individual MPC for more physically meaningful stochastic channel representation, where the clusters are formed by grouping scatterers that generate MPCs with similar delays and directions. For cluster-level stochastic channel modeling, automatic clustering algorithms are often used to identify clusters from the extracted MPCs. The K-powerMeans (KPM) clustering algorithm [60] is the most popular method. The iterative procedure of KPM is simply expressed as

- `Assign each MPC to cluster:`

$$I_l \leftarrow \arg\min_k \{P_l \cdot \texttt{MCD}(\boldsymbol{x}_l, \boldsymbol{c}_k)\} \tag{16}$$

- `Update cluster centroids:`

$$\boldsymbol{c}_k \leftarrow \frac{\sum_{j\in C_k} P_j \boldsymbol{x}_j}{\sum_{j\in C_k} P_j} \tag{17}$$

where $\boldsymbol{x}_l$ and $\boldsymbol{c}_k$ denote the l-th MPC with power of P_l and the k-th cluster centroid, respectively. The multipath component distance, $\texttt{MCD}(\boldsymbol{x}_i, \boldsymbol{x}_j) = \|\boldsymbol{x}_i - \boldsymbol{x}_j\|$ where $\boldsymbol{x}_l$ is the modified parameter vector having appropriately normalized elements which are constructed by a few different methods from $\boldsymbol{\mu}_l$ [60], [62], [63]. Here, we used the projection onto the azimuth plane as $\boldsymbol{x}_l = [\tau_l, \cos\phi_l, \sin\phi_l, \cos\phi_l', \sin\phi_l']$. The index I_l is the cluster number for the l-th MPC, and the set C_k contains the MPC indices belonging to the k-th cluster. The KPM algorithm iteratively minimizes the total sum of the power-weighted distance of a path to the given number of cluster centroids in (16), thereby minimizing the global spreads of the clusters.

The drawback of KPM is that it is necessary to predetermine the number of clusters, and the result totally depends on it. In practice, the optimum number of clusters is usually determined by any evaluation method such as Kim-Parks index, Calinski-Harabasz, Davies-Bouldin index, and score fusion [61]. The KPM result is not very robust and subject to the normalization of the modified parameter vector, threshold setup, and so on. In this regard, the CLEAN algorithm based method where the information of the number of clusters is unnecessary has also been proposed [62].

Here, for each measurement point, 100 MPCs were extracted. The residual power ratio by extracting the estimated 100 MPCs from the measured channel matrix was less than 20 % for LoS condition. The KPM was adopted to clusterize

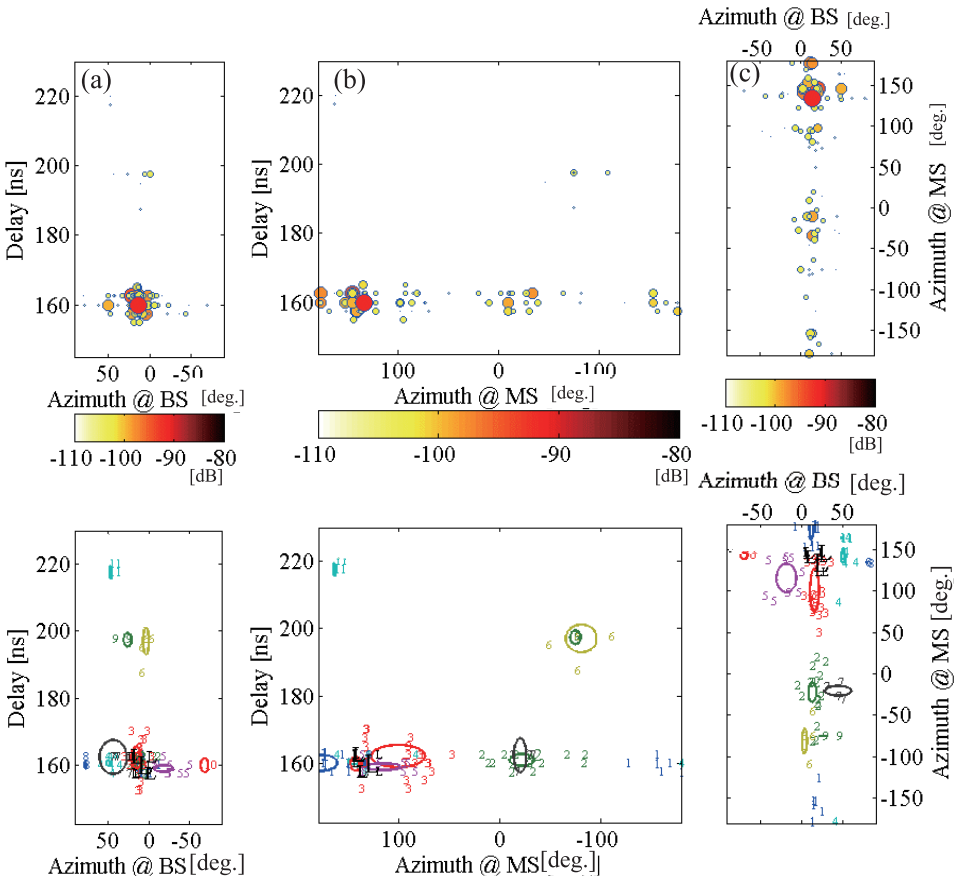

Fig. 16 Extracted MPCs and clustering results at #46 (LoS) in the upper and lower figures, respectively, where leftmost, center and rightmost figures illustrate the MPCs and the associated cluster numbers in azimuth-delay domain at BS and MS, and azimuth-azimuth domain, respectively.

the MPCs for each snapshot. Figure 16 shows an example of the extracted MPCs and the clustering results at #46 (LoS) in the upper and lower figures, respectively, where the leftmost, the center and the rightmost figures illustrate the MPCs and the associated cluster numbers in azimuth-delay domain at BS and MS, and azimuth-azimuth domain, respectively.

6. Channel Modeling

This section describes the statistical analysis of the large scale parameters (LSPs) and cluster parameters from the extracted MPCs and clusters. We derived them following the widely accepted WINNER/3GPP channel model [8], [9], and compared with 3GPP UMi model parameters.

6.1 Large Scale Parameters (LSPs)

Assuming MPCs are exponentially-distributed and exponentially-/uniformly-distributed in delay domain for LoS and NLoS conditions, respectively. The RMS (root mean square) delay spread (DS) that is calculated from a PDP by

$$\mathrm{DS} = \sqrt{\frac{\sum_l (\tau_l - \bar{\tau})^2 P_l}{\sum_l P_l}}, \text{where } \bar{\tau} = \frac{\sum_l \tau_l P_l}{\sum_l P_l} \tag{18}$$

is a commonly used parameter to represent the temporal dispersion of the channel. From Fig. 17(a) which was calculated based on the MPC parameters, it is seen that the values are significantly smaller than those of the 3GPP UMi model. Table 4 summarizes the statistical model parameters in detail. Assuming MPCs are wrapped Gaussian-distributed in azimuth angle domain both for LoS and NLoS conditions, the angular spread (AS) is obtained by

$$\mathrm{AS} = \min_{\Delta\phi} \left(\sqrt{\frac{\sum_l \left(f(\phi_l + \Delta\phi - \bar{\phi}) \right)^2 P_l}{\sum_l P_l}} \right), \tag{19}$$

where $\bar{\phi} = \frac{\sum_l f(\phi_l + \Delta\phi) P_l}{\sum_l P_l}$ and $f(y) = y \bmod 2\pi$, a wrapping function. The cumulative distribution functions (CDFs) of azimuth angular spreads of arrival and departure (ASD and ASA) are shown in Fig. 17(b) and Fig. 17(c), respectively. It should be noted that we follows the WINNER/3GPP convention of ASD and ASA being defined in downlink channel, i.e., departure refers to BS and arrival refers to MS, assuming the radio channel's reciprocity, even though the channel measurement was conducted in uplink. It can be seen that the distributions of ASD and ASA are very similar to those of the 3GPP UMi model.

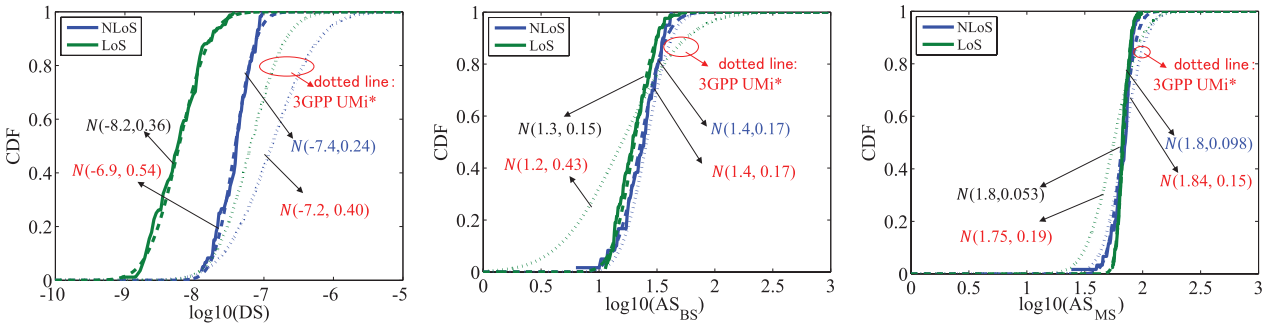

(a) Delay spread (DS). (b) Angle spread at BS (ASD). (c) Angle spread at MS (ASA).

Fig. 17 Inter-cluster parameters.

Table 4 Channel Model Parameters.

		11 GHz UMi		3GPP UMi [9]	
		NLoS	LoS	NLoS	LoS
Delay spread (DS)	μ	−7.4 (39.8 ns)	−8.2 (6.3 ns)	−6.89 (129 ns)	−7.19 (64.6 ns)
$\log_{10}$[sec]	σ	0.24	0.36	0.40	0.54
AoD spread (ASD)	μ	1.4 (25.1°)	1.3 (20.0°)	1.41 (25.7°)	1.2 (15.8°)
$\log_{10}$[°]	σ	0.17	0.15	0.17	0.43
AoA spread (ASA)	μ	1.8 (63.1°)	1.8 (63.1°)	1.84 (69.2°)	1.75 (56.2°)
$\log_{10}$[°]	σ	0.1	0.1	0.15	0.19
No. clusters		9	9	12	19
Cluster ASD		4.56	5.16	10	3
Cluster ASA		12.78	14.82	22	17
XPR	μ	7.9	7.8	8.0	9.0
[dB]	σ	3.8	4.2	3.0	3.0

6.2 Cluster Parameters

This subsection presents the statistical properties of the clusters, so called, cluster parameters. Figure 18(a) shows the CDFs of the numbers of clusters for LoS and NLoS conditions, respectively, which are nearly uniformly distributed between 5 and 20. In both cases, 9 clusters are detected in average, which is a slightly smaller number comparing with the 3GPP UMi model [9]. Further, Fig. 18(b) shows the CDFs of intra-cluster angular spread which is an important parameter for MIMO spatial multiplexing performance because it determines the size of a cluster. Comparing with the 3GPP UMi model, it can be seen that the AS at MS significantly decreases while the AS at BS are similarly distributed.

Figure 18(c) shows the cluster's polarization properties of cross-polarization power ratio (XPR) and co-polarization power ratio (CPR) [15] where the cluster XPR and CPR were characterized averaging those of all paths within a cluster. It can be seen that the distributions of them are very similar to those of 3GPP UMi model for both conditions of NLoS and LoS.

6.3 Channel Model Validation

From the channel model as described in previous subsections, a MIMO channel matrix was synthesized by the same recipe of the WINNER/3GPP channel models [8], [9]. In this section, the parameters presented in Table 4 were used, and the same values of the 3GPP UMi model were used for the other parameters which are not given in Table 4. Assuming the orthogonally dual-polarized 12-element UCAs at both sides of Tx and Rx which have been used in the measurement campaigns as shown in Fig. 12, the MIMO CTFs are expressed by cluster delay line (CDL) model as

$$\boldsymbol{H}(f) = \sum_{k=1}^{K} \sqrt{P_k} \sum_{l=1}^{L_k} \boldsymbol{A}'(\phi'_{k,l}) \boldsymbol{\Gamma}_{k,l} \boldsymbol{A}^T(\phi_{k,l}) e^{-\mathrm{j}2\pi f \tau_{k,l}}, \quad (20)$$

where P_k denotes the power of k-th cluster, and $\boldsymbol{A}(\phi_{k,l})$ and $\boldsymbol{A}'(\phi'_{k,l})$ denote the dual-polarized antenna pattern matrices for the Tx (BS) and Rx (MS), respectively. $\phi_{k,l}$ and $\phi'_{k,l}$ indicate the azimuth angles at the Tx and the Rx for the l-th path of the k-th cluster. The complex path weight is generated by $\boldsymbol{\Gamma}_{k,l} = \begin{bmatrix} e^{\mathrm{j}\Phi^{\mathrm{VV}}_{k,l}} & \sqrt{\kappa_{k,l}} e^{\mathrm{j}\Phi^{\mathrm{VH}}_{k,l}} \\ \sqrt{\kappa_{k,l}} e^{\mathrm{j}\Phi^{\mathrm{HV}}_{k,l}} & e^{\mathrm{j}\Phi^{\mathrm{HH}}_{k,l}} \end{bmatrix}$ where $\kappa_{k,l}$ denotes the XPR, and $\Phi^{\mathrm{VV}}_{k,l}, \Phi^{\mathrm{VH}}_{k,l}, \Phi^{\mathrm{HV}}_{k,l}, \Phi^{\mathrm{HH}}_{k,l}$ are uniformly distributed random initial phases.

The channel model was evaluated by the open loop ergodic MIMO capacity for a particular signal-to-noise ratio (SNR), η_i, as

$$C = E\left(\log_2 \det\left[\boldsymbol{I}_{N_\mathrm{R}} + \frac{\eta_i}{N_\mathrm{T}} \boldsymbol{H}\boldsymbol{H}^H\right]\right) \quad (21)$$

where $\boldsymbol{H}$ is normalized so that $\|\boldsymbol{H}\|_F^2 = N_\mathrm{T} N_\mathrm{R}$. On the other

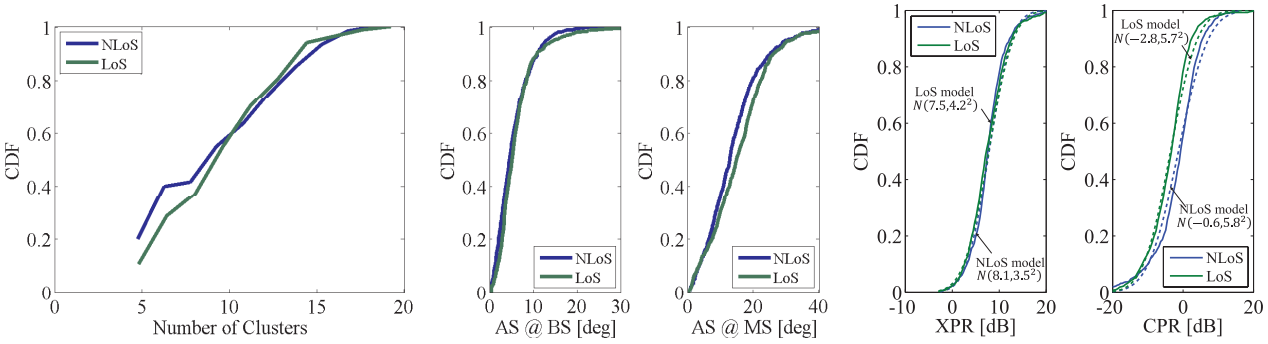

(a) Number of clusters. (b) Intra cluster angle spreads. (c) XPR and CPR.

Fig. 18 Cluster parameters.

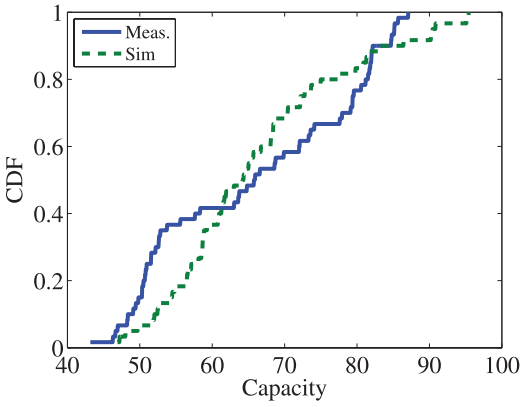

(a) Capacity.

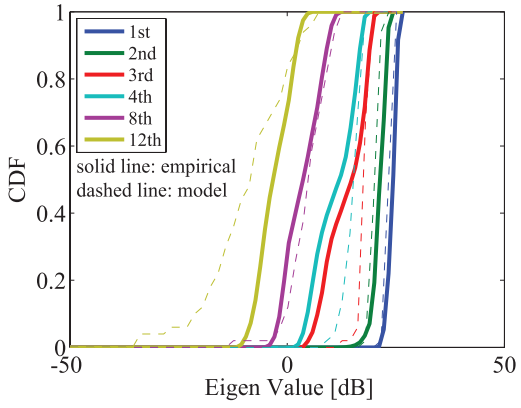

(b) Eigenvalues.

Fig. 19 Channel model validation in NLoS condition.

hand, the eigenvalues were derived to investigate the accuracy of the eigen-space of the synthesized MIMO channel matrices. Figure 19 illustrates the comparison of the channel capacity and eigenvalue distributions in NLoS condition where the solid and dashed lines denote the empirical distribution and the distribution generated by the channel model.

From Fig. 19(b), the distribution obtained from the channel model is relatively well matched to the empirical distribution for its irregular shape. On the other hand, regarding the eigen values in Fig. 19(b), the larger discrepancy (under-estimated) is found for the higher order eigen values which usually have minor contribution in the performance. It should be noted that the channel model parameters are statistically obtained using the MPCs extracted by the parameter estimation, where the extracted MPCs are mostly generated by dominant specular reflection, but other possible mechanisms with minor contribution cannot be perfectly represented in this model.

7. Discussion

From measurement results described above, it is seen that the channels at 11 GHz are less dispersive in delay domain but have similarly spread in angle domain. It is also seen that the cluster is less spread in angle domain. However, those are still an early conclusion, and careful validation and comparative study with those at other frequencies will be necessary clarifying frequency dependency.

In fact, in 5G channel modeling a new requirement is that the model should be valid for the wide range of frequencies up to 100 GHz, and should also have scalability and reasonable complexity compatible to existing standard models [10], [33]. In order to develop such a model, extensive measurement and validation by simulation should be conducted. Compiling large amount of results, more accurate generic and site-specific channel models applicable to the wide target frequency range should be developed.

For high frequency channel modeling, the treatment of diffuse scattering caused by rough surface of scattering objects is a still open issue in that the interaction by scattering objects may be influenced depending on the wavelength of the signal, but we do not actually have any clear conclusion yet. From measurement, diffuse scattering is often extracted as a dense multipath component (DMC) which cannot be separable from the measured channel response as a specular multipath component (SMC). Currently, the characterization and modeling of DMC is on-going [64], which will provide

more accurate estimation of transmission performance.

From the radio channel measurement viewpoint, a fast and super-high resolution channel acquisition are challenging. As described above, in high frequency radio transmission systems, small coverage area will be used to increase transmission rates resolving very high transmission attenuation. However, due to very short wavelength, even relatively small obstacles such as people and furniture can cause severe shadowing to the high frequency radio links. Therefore, modeling dynamic characteristics of human-blockage and multipath behavior that are characterized by fast channel acquisition should be very important to design the system much reliable. In addition, a super-high resolution directional property should be required because the angular domain accuracy for individual MPCs within a cluster needs to be much more improved (less than 1 degree [33]) to properly model sub-path behavior in more detail for an advanced multi-antenna technique such as massive MIMO [65].

8. Conclusion

This paper provided a useful tutorial of a whole procedure of channel modeling; multi-dimensional channel sounding, propagation channel measurement, analysis and modeling, which may be practically useful for various radio propagation/communication researchers and engineers to begin field measurement. First, this paper overviewed the fundamentals of MIMO channel sounding and then provided a practical example of developed MIMO channel sounders in a fully parallel scalable architecture for the high frequency bands of 11 GHz and 60 GHz. Then, the measurement campaigns in outdoor UMi at 11 GHz and data processing were introduced, and the cluster based channel analysis was presented with brief description on commonly used methods for MPC extraction and automatic clustering. Finally, the channel parameters are derived and the developed model was validated with channel capacity and eigenvalue distribution with actual antenna arrays. Finally, related current and future channel modeling issues were discussed.

Acknowledgments

This work was partly supported by “The research and development project for expansion of radio spectrum resources” and “The Strategic Information and Communications R&D Promotion Program (SCOPE: No.145004102)” of The Ministry of Internal Affairs and Communications (MIC), Japan, and “JSPS KAKENHI (Grant Number: 15H04003)”.

References

[1] “Resolution COM6/20 (WRC-15),” Provisional Final Acts World Radio Communication Conference (WRC-15), pp.424–428, Nov. 2015.
[2] T. Rappaport, S. Sun, R. Mayzus, H. Zhao, Y. Azar, K. Wang, G.N. Wong, J.K. Schulz, M. Samimi, and F. Gutierrez, “Millimeter wave mobile communications for 5G cellular: It will work!,” IEEE Access, vol.1, pp.335–349, 2013.
[3] J. Medbo, K. Borner, K. Haneda, V. Hovinen, T. Imai, J. Järvelainen, T. Jämsa, A. Karttunen, K. Kusume, J. Kyrölainen, P. Kyösti, J. Meinilä, V. Nurmela, L. Raschkowski, A. Roivainen, and J. Ylitalo, “Channel modelling for the fifth generation mobile communications,” Proc. Eur. Conf. Antennas Propag. (EuCAP), April 2014.
[4] MiWEBA, FP7 ICT-2013-EU-Japan, http://www.miweba.eu
[5] G. Calcev, D. Chizhik, B. Goransson, S. Howard, H. Huang, A. Kogiantis, A. Molisch, A. Moustakas, D. Reed, and H. Xu, “A wideband spatial channel model for system-wide simulations,” IEEE Trans. Veh. Technol., vol.56, no.2, pp.389–403, 2007.
[6] R. Verdone and A. Zanella, Pervasive Mobile and Ambient Wireless Communications: COST Action 2100, Springer, 2012.
[7] N. Cardona, Cooperative Radio Communications for Green Smart Environments, River Publishers Series in Communications, June 2016.
[8] IST-4-027756 WINNER II D1.1.2 V1.2. (2008, Feb.) WINNER II Channel Models. [Online]. Available: http://www.ist-winner.org
[9] 3GPP, Technical specification group radio access network; Evolved Universal Terrestrial Radio Access (E-UTRA); Further advancements for E-UTRA physical layer aspects. TR 36.814 (release 9), 3GPP, 2010.
[10] K. Haneda, L. Tan, Y. Zheng, H. Asplund, J. Li, Y. Wang, D. Steer, C. Li, T. Balercia, S. Lee, Y. Kim, A. Ghosh, T. Thomas, T. Nakamura, Y. Kakishima, T. Imai, H. Papadopoulos, T.S. Rappaport, G.R. MacCartney, M.K. Samimi, S. Sun, O. Koymen, S. Hur, J. Park, C. Zhang, E. Mellios, A.F. Molisch, S.S. Ghassamzadeh, and A. Ghosh, “5G 3GPP-like channel models for outdoor urban microcellular and macrocellular environments,” Proc. IEEE Veh. Technol. Conf. (VTC), May 2016.
[11] 3GPP, Technical specification group radio access network; Study on channel model for frequency spectrum above 6 GHz. TR 38.900, 3rd Generation Partnership Project (3GPP), June 2016.
[12] J. Takada, Y. Konishi, B. Gao, M. Kim, M. Ghoraishi, S. Suyama, and H. Suzuki, “Development of 4x4 full-MIMO channel sounder operating at 11 GHz with 400 MHz bandwidth utilizing software radio architecture,” Proc. URSI GASS, Aug. 2011.
[13] S. Suyama, J. Shen, Y. Oda, H. Suzuki, and K. Fukawa, “11 GHz band 8x16 MIMO-OFDM outdoor transmission experiment for 10 Gbps super high bit rate mobile communications,” IEEE Inter. Symp. on Personal Indoor Mobile Radio Commun. (PIMRC), Sept. 2013.
[14] S. Suyama, J. Shen, H. Suzuki, K. Fukawa, and Y. Okumura, “Evaluation of 30 Gbps super high bit rate mobile communications using channel data in 11 GHz band 24x24 MIMO experiment,” Proc. IEEE Int. Conf. Commun., May 2014.
[15] M. Kim, Y. Konishi, Y. Chang, and J. Takada, “Large scale parameters and double-directional characterization of indoor wideband radio multipath channels at 11 GHz,” IEEE Trans. Antennas Propag., vol.62, no.1, pp.430–441, Jan. 2014.
[16] M. Kim, J. Takada, Y. Chang, J. Shen, and Y. Oda, “Large scale characteristics of urban cellular wideband channels At 11 GHz,” Proc. Eur. Conf. Antennas Propag. (EuCAP), April 2015.
[17] J. Takada, M. Kim, and K. Saito, “Characterization of radio propagation channel at 11 GHz,” Proc. European Wireless, May 2016.
[18] A. Molisch and F. Tufvesson, “Propagation channel models for next-generation wireless communications systems,” IEICE Trans. Commun., vol.E97-B, no.10, pp.2022–2034, Oct. 2014.
[19] S. Salous, V. Degliesposti, M. Nekovee, and S. Hur, “Millimeter-wave propagation characterization and modelling towards 5G systems,” Proc. Eur. Conf. Antennas Propag. (EuCAP), April 2015.
[20] A. Molisch, Wireless Communications, 2nd ed., Willey, 2011.
[21] K. Haneda, “Channel models and beamforming at millimeter-wave frequency bands,” IEICE Commun., vol.E98-B, no.5, pp.755–772, May 2015.
[22] M. Steinbauer, A.F. Molisch, and E. Bonek, “The double-directional radio channel,” IEEE Antennas Propag. Mag., vol.43, no.4, pp.51–63, Aug. 2001.
[23] RUSK Channel Sounder, MEDAV, http://www.channelsounder.de
[24] Elektrobit Radio Channel Sounder, EB Propsound, http://www.

elektrobit.com
[25] E-1130 MIMO Channel Sounder, KODEN Electronics Co. Ltd., https://www.koden-electronics.co.jp/en
[26] G. Gutierrez, O. Gonzalez, J. Perez, D. Ramirez, L. Vielva, J. Ibanez, and I. Santamaria, "Frequency-domain methodology for measuring MIMO channels using a generic test bed," IEEE Trans. Instrum. Meas., vol.60, no.3, pp.827–837, March 2011.
[27] B. Maharaj, J. Wallace, M. Jensen, and L. Linde, "A Low-cost open-hardware wideband multiple-input-multiple-output (MIMO) wireless channel sounder," IEEE Trans. Antenna Propag., vol.57, no.10, pp.2285–2289, Oct. 2008.
[28] V. Kolmonen, J. Kivinen, L. Vuokko, and P. Vainikainen, "5.3-GHz MIMO radio channel sounder," IEEE Trans. Instrum. Meas., vol.55, no.4, pp.1263–1269, Aug. 2006.
[29] Y. Konishi, Y. Chang, M. Kim, and J. Takada, "Versatile radio channel sounder for double directional and multi-link MIMO channel measurements at 11 GHz," IEICE Trans. Electron., vol.E97-C, no.10, pp.994–1004, Oct. 2014.
[30] S. Salous, S.M. Feeney, X. Raimundo, and A.A. Cheema, "Wideband MIMO channel sounder for radio measurements in the 60 GHz band," IEEE Trans. Wireless Commun., vol.15, no.4, pp.2825–2832, April 2016.
[31] M. Kim, H. Pham, and J. Takada, "Development of low-cost 60-GHz millimeter-wave MIMO channel sounding system," Proc. 6th Global Symposium of Millimeter Waves (GSMM), April 2013.
[32] 3GPP: 'Evolved Universal Terrestrial Radio Access (E-UTRA); Physical Channels and Modulation (Release 10)', TS 36.211 V10.1.0 (2011-03).
[33] S Jaeckel, M. Peter, K. Sakaguchi, W. Keusgen, and J. Medbo, "5G channel models in mm-wave frequency bands," Proc. European Wireless, May 2016.
[34] S. Boyd, "Multitone signals with low crest factor," IEEE Trans. Circuits Syst., vol.33, no.10, pp.1018–1022, Oct. 1986.
[35] D. Chu, "Polyphase codes with good periodic correlation properties," IEEE Trans. Inf. Theory, vol.IT-18, no.4, pp.531–532, July 1972.
[36] H. Dym and H. McKean, Fourier Series and Integrals, Academic Press, 1972.
[37] B. Popovic, "Efficient DFT of Zadoff-Chu sequences," Electron. Lett., vol.46, no.7, pp.502–503, April 2010.
[38] M. Kim, J. Takada, and Y. Konishi, "Novel scalable MIMO channel sounding technique and measurement accuracy evaluation with transceiver impairments," IEEE Trans. Instrum. Meas., vol.61, no.12, pp.3185–3197, Dec. 2012.
[39] K. Sakaguchi, J. Takada, and K. Araki, "A novel architecture for MIMO spatio-temporal channel sounder," IEICE Trans. Electron., vol.85-C, no.3, pp.436–441, March 2002.
[40] R. Pirkl and G. Durgin, "Optimal sliding correlator channel sounder design," IEEE Trans. Wireless Commun., vol.7, no.9, pp.3488–3497, Sept. 2008.
[41] M. Kim, H. You, and H. Lee, "A novel transmit scheme in CDM-based MIMO channel sounding systems," IEICE Trans. Commun., vol.E93-B, no.9, pp.2428–2432, Sept. 2010.
[42] S. Salous, R. Lewenz, I. Hawkins, N. Razavi-Ghods, and M. Abdallah, "Parallel receiver channel sounder for spatial and MIMO characterisation of the mobile radio channel," Proc. IEE Commun., vol.152, no.6, pp.912–918, Dec. 2005.
[43] K. Mizutani, K Sakaguchi, J. Takada, and K. Araki, "Development of MIMO-SDR platform and its application to real-time channel measurements," IEICE Trans. Commun., vol.E89-B, no.12, pp.3197–3207, Dec. 2006.
[44] K. Wangchuk, K. Umeki, T. Iwata, P. Hanpinitsak, M. Kim, K. Saito, and J. Takada, "Double directional millimeter wave propagation channel measurement and polarimetric cluster properties in outdoor urban pico-cell environment," IEICE Trans. Commun., vol.E100-B, no.7, pp.1133–1144, July 2017.
[45] M. Kim, K. Umeki, K. Wangchuk, J. Takada, and S. Sasaki, "Polarimetric mm-wave channel measurement and characterization in a small office," Proc. IEEE Symp. Per. Indoor Mobile Radio Commun. (PIMRC), Aug. 2015.
[46] M. Kim, K. Umeki, T. Iwata, K. Wangchuk, J. Takada, and Sh. Sasaki, "Simulation based mm-wave channel model for outdoor open area access scenarios," Proc. URSI Asia-Pacific Radio Science Conference (URSI AP-RASC), Aug. 2016.
[47] M. Kim, T. Iwata, K. Umeki, K. Wangchuk, J. Takada, and S. Sasaki, "Mm-wave outdoor-to-indoor channel measurement in an open square smallcell scenario," Proc. International Symposium on Antennas and Propagation (ISAP), Oct. 2016.
[48] D. Lee, H. Seo, and B. Clerckx, "Coordinated multipoint transmission and reception in LTE-advanced: Deployment scenarios and operational challenges," IEEE Commun. Mag., pp.148–155, Feb. 2012.
[49] C. Oestges, "Multi-link propagation modeling for beyond next generation wireless," Proc. Loughborough Antennas and Propagation Conf. (LAPC), Nov. 2011.
[50] "Cesium frequency standard, Microsemi," [Online]. Available: http://www.microsemi.com/products/timing-synchronization-systems/time-frequency-references/cesium-frequency-standards/5071a
[51] G Fettweis, M. Lohning, D. Petrovic, M. Windisch, P. Zillmann, and W. Rave, "Dirty RF: A new paradigm," Proc. IEEE Symp. Per., Indoor Mobile Radio Commun. (PIMRC), Sept. 2005.
[52] M. Valkama, M. Renfors, and V. Koivunen, "Advanced methods for IQ imbalance compensation in communication receivers," IEEE Trans. Signal Process., vol.49, no.10, pp.2335–2344, Oct. 2001.
[53] L. Anttila, M. Valkama, and M. Renfors, "Frequency-selective I/Q mismatch calibration of wideband direct-conversion transmitters," IEEE Trans. Circuits Syst. II, vol.55, no.4, pp.359–363, April 2008.
[54] M. Kim, Y. Maruichi, and J. Takada, "Parametric method of frequency-dependent I/Q imbalance compensation for wideband quadrature modulator," IEEE Trans. Microw. Theory Techn., vol.61, no.1, pp.260–270, Jan. 2013.
[55] A. Taparugssanagorn and J. Ylitalo, "Characteristics of short-term phase noise of MIMO channel sounding and its effect on capacity estimation," IEEE Trans. Instrum. Meas., vol.58, no.1, pp.196–201, Jan. 2009.
[56] 60 GHz Waveguide Development System, V60WGD02, http://www.vubiq.com
[57] Multipath Propagation and Parameterization of Its Characteristics, Recommendation ITU-R P.1407-4, IUT-R, Oct. 2009.
[58] B.H. Fleury, M. Tschudin, R. Heddergott, D. Dahlhaus, and K.I. Pedersen, "Channel parameter estimation in mobile radio environments using the SAGE algorithm," IEEE J. Sel. Areas Commun., vol.17, no.3, pp.434–450, March 1999.
[59] A. Richter and R.S. Thoma, "Joint maximum likelihood estimation of specular paths and distributed diffuse scattering," Proc. 61st IEEE Veh. Technol. Conf. (VTC-Spring), vol.1, pp.11–15, Stockholm, Sweden, May 2005.
[60] N. Czink, P. Cera, J. Salo, E. Bonek, J.P. Nuutinen, and J. Ylitalo, "A framework for automatic clustering of parametric MIMO channel data including path powers," Proc. IEEE Veh. Technol. Conf. (VTC), Sept. 2006.
[61] L. Materum, J. Takada, I. Ida, and Y. Oishi, "Mobile station spatiotemporal multipath clustering of an estimated wideband MIMO doubledirectional channel of a small urban 4.5 GHz macrocell," Eurasip J. Wireless Commun. and Networking, vol.2009, no.1, 2009.
[62] X. Yin, C. Ling, and M. Kim, "Experimental multipath-cluster characteristics of 28-GHz propagation channel," IEEE Access, vol.3, pp.3138–3150, 2015.
[63] P. Hanpinitsak, K. Saito, J. Takada, M. Kim, and L. Materum, "Clustering method based on scatterer locations for indoor dynamic MIMO channel," Proc. Eur. Conf. Antennas Propag. (EuCAP), April 2016.
[64] K. Saito, M. Kim, and J. Takada, "Dense multipath component parameter estimation in 11 GHz-band indoor environment," Proc. IEEE Symp. Per., Indoor Mobile Radio Commun. (PIMRC), Sept. 2016.

[65] F. Rusek, D. Persson, B. Lau, E. Larsson, T. Marzetta, O. Edfors, and F. Tufvesson, "Scaling up MIMO: Opportunities and challenges with very large arrays," IEEE Signal Process. Mag., vol.30, no.1, pp.40–60, Jan. 2013.

Minseok Kim was born in Seoul, Korea. He received the B.S. degree in Electrical Engineering from Hanyang University, Seoul, Korea, M.E. and D.E. degrees in Division of Electrical and Computer Engineering, Yokohama National University (YNU), Japan in 1999, 2002 and 2005, respectively. He has been with Tokyo Institute of Technology from 2007 as an assistant professor. He has been on leave to Georgia Institute of Technology as a visiting scholar in 2010. From 2014, he joined Graduate School of Engineering, Niigata University, Niigata, Japan as an associate professor. His research interests include radio propagation channel measurement and modeling, body area network, antenna array signal processing, DSP implementation on FPGAs, and cognitive and software defined radios. Dr. Kim received the Young Researcher's Encouragement Award of IEEE VTS Japan and the Telecommunications Advancement Foundation (TAF) Telecommunications System Technology Encourage Award in 2003 and 2014, respectively. He is members of IEEE and IEIE.

Jun-ichi Takada received the B.E., M.E. and D.E. degrees from Tokyo Institute of Technology, Japan in 1987, 1989 and 1992, respectively. He was a research associate at Chiba University, Japan, from 1992 to 1994. Since 1994 to 2006, he was an associate professor at Tokyo Institute of Technology, and from 2006, he became a professor. From 2003 to 2007, he was also a researcher at the National Institute of Information and Communications Technology, Japan. From 2007 to 2010, he was a co-chair of special interest group E on body communications within EU COST Action 2100. His current interests include radio-wave propagation and channel modeling for various wireless systems, regular issues of spectrum sharing, and ICT applications for international development. Dr. Takada received Achievement Award of IEICE in 2008, and he has been appointed as an IEICE Fellow in 2012.

Kentaro Saito was born in Kanagawa, Japan, in 1977. He received his B.S. and Ph.D. degrees from The University of Tokyo, Japan, in 2002 and 2008, respectively. He joined NTT DOCOMO, Kanagawa, Japan, in 2002. Since then, he has been engaged in the research and development of mobile communication systems, and the radio propagation. He joined Tokyo Institute of Technology, Japan in 2015. Since then, he has been engaged in the research of radio propagation for mobile communication systems. Dr. Saito is Members of IEICE and IEEE.